 CMC, vol.8, no.3, pp.151-164, 2009

Modelling a Plunging Breaking Solitary Wave with Eddy-Viscosity Turbulent SPH Models

R. Issa[1] **and D. Violeau**[1]

Abstract: Breaking waves can run up at the shoreline, inundating coastal regions and causing large property damage and loss of life. In order to proceed to the design of sea defence structures and estimate the possible damage resulting from sea submersion due to a tsunami for instance, it is thus crucial to understand these phenomena. However, due to the mathematical difficulties caused by the complexities of the fluid motion associated with breaking wave, a fully theoretical approach is not possible. Thus most of the investigations regarding breaking waves are experimental and numerical. Some methods were recently developed to perform such simulations, among them Volume Of Fluids (VOF) and Lagrangian methods. In this paper, the gridfree Smoothed Particle Hydrodynamics (SPH) is used. SPH is preferencially used in CFD to simulate complex flows with one or several convoluted free surfaces. Indeed, this type of flows would require distorted meshes with Eulerian finite difference methods or very fine meshes with VOF. The ability of SPH to reproduce a plunging breaking solitary wave and to simulate the different stages of its process is herein investigated. Since breaking waves are characterised by high distorsion, turbulence modelling plays a crucial role in such simulations. Therefore, the turbulence models developed by the authors and presented in earlier publications [Violeau and Issa (2006)] are here applied. The results, compared to experiments, are on the whole satisfactory, specially the simulation of the splashup phenomenon. Moreover, it is shown that turbulence modelling has a strong influence on the quality of the results.

Keyword: SPH, solitary wave, plunging breaking wave, statistical turbulence modelling.

[1] EDF R&D, LNHE, Chatou, FRANCE.

1 Introduction

The ocean waves generated by seismic events usually have long wavelengths and small wave heights. As they propagate shoreward, due to the offshore bathymetry, the wave heights can increase significantly, leading to breaking waves near the shoreline [Li and Raichlen (2003)]. These breaking waves can run up at the shoreline, inundating coastal regions and causing large property damage and loss of life. In order to proceed to the design of sea defence structures and estimate the possible damage resulting from sea submersion due to a tsunami for instance, it is thus crucial to understand these phenomena. The complexity of the problem and its theoretical intractability are obvious in figure 4. Thus, most of investigations for breaking waves are experimental and numerical. Some methods were recently developed to perform such simulations, among them Volume Of Fluids (VOF) and Lagrangian methods. After its development for astrophysics applications, SPH has successfully been applied in fluid mechanics to simulate delicate free surface flows (dam breaking, wave flumes, etc.) which would require complex meshes with classical Eulerian codes. SPH is also very efficient for rapid, convection dominated flows. For the purpose of presented simulations, since highly distorted flow are presented, turbulence modelling plays a crucial role. However, turbulence developments in SPH are rather recent and still not generalized, although some stochastic approaches have been tested [Welton (1998)], [Violeau, Picon, and Chabard (2002)]. Unfortunately, they are quite complex and time consuming. Some recent improvements have been achieved during the past few years: the authors developed a SPH mixing length model [Issa (2004)], as well as k and k-ε

models [Violeau and Issa (2006)]. In the meanwhile, Lo and Shao developed 2D SPH Large Eddy Simulation [Lo and Shao (2002)], also applied in [Dalrymple and Rogers (2006)]. The authors [Issa (2004)] also investigated 3D Large Eddy Simulation with success. One should emphasize the fact that many authors still neglect turbulence modelling in SPH and consider a constant eddy viscosity. Contrary to this approach, the authors [Violeau and Issa (2006)] have experienced that turbulence closures based on the concept of eddy viscosity (namely mixing length, k and $k-\varepsilon$ models) provide both physical accuracy and numerical smoothness. We apply in this paper several of these models to the simulation of a plunging breaking solitary wave and reveal that turbulent effects must be taken into account for modelling such phenomena.

2 Statistical turbulence modelling

Turbulent flows are omnipresent in nature and are characterised by chaotic fluctuations of pressure and velocity components, which play a crucial role in increasing momentum diffusion. The simplest way to investigate turbulent flows is to time-average unsteady fluctuations, hence achieving turbulence statistical modelling. Only averaged values defined by ensemble, time or spatial averaging [Métais (2001)] are considered; by applying the average operator $\langle\ \rangle$ to the Navier-Stokes equations, one ends up with the Reynolds equations (1894) (see e.g. [Pope (2000)]).

2.1 Eulerian Reynolds equations

In an Eulerian formalism, the Reynolds continuity equation is written

$$\frac{\partial \rho}{\partial t}+\frac{\partial \langle \rho u_i \rangle}{\partial x_i}=0 \tag{1}$$

When considering nearly incompressible flows (characterised by density fluctuations less than 1 %), terms due to fluid compressibility could be neglected in the Reynolds momentum equation which then reads

$$\frac{d\langle u_i\rangle}{dt}=\frac{\partial \langle u_i\rangle}{\partial t}+\langle u_j\rangle\frac{\partial \langle u_i\rangle}{\partial x_j}=-\frac{1}{\rho}\frac{\partial \langle p\rangle}{\partial x_i} + \nu\frac{\partial^2\langle u_i\rangle}{\partial x_j\partial x_j}-\frac{\partial R_{ij}}{\partial x_j}+F_i^e \tag{2}$$

with a summation over j subscript (Einstein's conventions), where i varies from 1 to 3 in 3D and from 1 to 2 in 2D. $\langle . \rangle$ denotes average values, $\langle u_i\rangle$ corresponds to the $i-$component of the averaged velocity and R_{ij} are the components of the Reynolds stress tensor defined by $R_{ij}=\left\langle u_i'u_j'\right\rangle$, $u_i'\equiv u_i-\langle u_i\rangle$ being the velocity fluctuating component satisfying $\langle u_i'\rangle=0$. p, ρ and ν respectively denote pressure, density and kinematic viscosity while F_i^e corresponds to the i-component of an external volumetric force, *e.g.* the gravity. The Reynolds stress tensor incorporates the influence of the removed turbulence fluctuations on the mean flow and describes the influence of all scales of turbulent motion, including the anisotropic large scales [Eggels (1994)] and need to be estimated from physical considerations, which consist of the so-called "turbulent closure model". In the following, we will consider first order closure models, meaning that the Reynolds stresses are directly related to kinematic averaged quantities. In equation (2), this tensor acts as a diffusion term quantifying turbulence mixing.

2.2 The eddy viscosity assumption

In order to close the equation set relative to (1) and (2), several techniques allow to express the Reynolds stress values in term of the resolved quantities: the more commonly used family of models is based on the eddy viscosity assumption, introduced by Boussinesq in 1880 [Pope (2000)]. In laminar flows, energy dissipation, transport of mass and momentum are all mediated by the viscosity. Since these phenomena are enhanced by turbulence, it is thus natural to assume that turbulent effects can be represented by an increased viscosity ν_T, which models the diffusion and dissipation properties of eddies. The average field stability is then ensured by this eddy viscosity ν_T, generally much higher than the fluid molecular

viscosity. An important feature of the eddy viscosity is that, conversely to the molecular viscosity, it is not a property of a given fluid but depends on the local turbulent characteristics. The eddy viscosity assumption consists in writing Reynolds stresses as

$$R_{ij} = \frac{2}{3}k\delta_{ij} - 2\nu_T \langle s_{ij} \rangle \tag{3}$$

where $k = \left\langle u_i' u_i' \right\rangle / 2$ denotes the turbulent kinetic energy (per mass unit), δ_{ij} is the Kronecker's symbol and $\langle s_{ij} \rangle$ the components of the rate of strain tensor based on averaged velocities

$$\langle s_{ij} \rangle = \frac{1}{2}\left(\frac{\partial \langle u_i \rangle}{\partial x_j} + \frac{\partial \langle u_j \rangle}{\partial x_i} \right) \tag{4}$$

With this model, the averaged momentum equation (2) is commonly approximated by

$$\frac{d\langle u_i \rangle}{dt} = -\frac{1}{\rho}\frac{\partial \langle p \rangle}{\partial x_i} + \frac{\partial}{\partial x_j}\left(2\left(\nu + \nu_T\right) \left\langle s_{ij} \right\rangle \right) + F_i^e \tag{5}$$

in which the turbulent kinetic energy k has been incorporated into the pressure term for convenience. In the following, we will restrict our considerations to eddy-viscosity-based models. As the eddy viscosity characterises the turbulent properties of the flow, it is thus not constant and has to be estimated.

2.3 Mixing length model

The simplest (and historically the first) model to estimate the eddy viscosity ν_T introduces the "mixing length" assumption, such that the eddy viscosity can be written

$$\nu_T = L_m u_t \tag{6}$$

where u_t denotes the typical velocity of large eddies and L_m a mixing length representing the characteristic distance of large eddy diffusive action [Lesieur (1997)]. An important assumption of the mixing length model is the balance between production and dissipation of the turbulent kinetic energy (see later equation (9)) and finally gives

$$\nu_T = L_m^2 S \tag{7}$$

where $S = \sqrt{2\langle s_{ij} \rangle \langle s_{ij} \rangle}$. In its generalised form (7), the mixing length model is applicable to all turbulent flows [Pope (2000)], provided the mixing length L_m is known, which is the major drawback of this model. For a complex flow such as a breaking wave, the specification of L_m requires a large measure of guesswork and consequently, one should have little confidence in the accuracy of the results. Morever, the assumption that production balances dissipation is not true for unsteady flows and close to walls and free surfaces [Viollet, Chabard, Esposito, and Laurence (1998)].

2.4 k model

The k model is also based on the mixing length assumption (6). However, the velocity u_t is here estimated through the turbulent kinetic energy k and gives

$$\nu_T = C_\mu \frac{k^2}{\varepsilon} \tag{8}$$

where $C_\mu = 0.09$ [Launder and Spalding (1972)]. In order to estimate the values of k, a transport equation is solved. The exact one for the turbulent kinetic energy is too complex to be directly solved [Métais (2001)] and after modelling the diffusion and the production term of this equation, it is commonly written

$$\frac{\partial k}{\partial t} + \underbrace{\langle \mathbf{u} \rangle . \nabla k}_{advection} = \underbrace{\nabla . \left[\left(\nu + \frac{C_\mu}{\sigma_k}\frac{k^2}{\varepsilon} \right) \nabla k \right]}_{diffusion} + \underbrace{P}_{production} - \underbrace{\varepsilon}_{dissipation} \tag{9}$$

The parameter σ_k corresponds to a Schmidt number and is equal here to 1.0 while C_μ equals to 0.09. The production term P is usually modelled by

$$P = C_\mu \frac{k^2}{\varepsilon} S^2 \tag{10}$$

However, this relation overestimates turbulent kinetic energy k for highly distorted flows where production should become linear with respect to the rate-of-strain. To circumvent this weakness,

one can use the following relation [Guimet and Laurence (2002)]

$$P = min\left(\sqrt{C_\mu}, C_\mu \frac{k}{\varepsilon} S\right) kS \tag{11}$$

The ε value is then obtained through the following relation

$$\varepsilon = C_\mu^{3/4} \frac{k^{3/2}}{L_m} \tag{12}$$

This model is well suited for unsteady flows, for which the energy production is characterised by a time scale $\tau \approx k/\varepsilon$ comparable to the timescale of the mean flow, like in wave propagation: contrary to the mixing length model, the k-model takes into account this transfer time. Once again, the drawback of this model is the mixing lenth definition requirement.

3 The SPH method

3.1 SPH formalism

In SPH formalism, the fluid is discretized with a finite number of macroscopic fluid volumes called "particles". Each particle a is characterised by a mass m_a, a density ρ_a, a pressure p_a, a velocity vector $\mathbf{u}_a$ and a position vector $\mathbf{r}_a$ among other quantities. In the following, all notations A_a will refer to quantity A corresponding to particle a. At the heart of SPH is the exact formula (13) which evaluates the value of any flow property A at the position $\mathbf{r}$ by

$$A(\mathbf{r}) = \int_\Omega A(\mathbf{r}')\delta(\mathbf{r}-\mathbf{r}')dr' \tag{13}$$

The previous summation is extended to the domain of interest Ω. For numerical reasons, the Dirac distribution δ is firstly approximated by a smooth kernel function w_h:

$$A(\mathbf{r}) = \int_\Omega A(\mathbf{r}')w_h(\mathbf{r}-\mathbf{r}')dr' + O\left(h^2\right) \tag{14}$$

The interpolating function w_h plays a central part in SPH: it depends on the distance between two particles (for a spherical kernel) and a parameter h called the smoothing length, proportional to the initial particle spacing. The transition to a discrete domain is achieved by approximating the integral of equation (14) by a Riemann summation:

$$A(\mathbf{r}) = \sum_b \frac{m_b}{\rho_b} A_b w_h(|\mathbf{r}-\mathbf{r}_b|) + O(h^2) \tag{15}$$

where A_b denotes the value of A at the point occupied by the particle b. The volume element dr' has been replaced by the particle volume m_b/ρ_b. The value of the function A relative to the particle a located at the point $\mathbf{r}$ is then expressed by

$$A_a = \sum_b \frac{m_b}{\rho_b} A_b w_h(r_{ab}) + O(h^2) \tag{16}$$

where r_{ab} denotes the distance between particles a and b. This summation is extended to all particles b that constitute the domain. In order to reduce the number of particles b involved in equation (15) (and thus to reduce the computing time), it is convenient to consider kernels characterised by a compact support of radius h_t, proportional to the smoothing length h. Consequently, only particles b located in the sphere of radius h_t and centred on a will contribute to the evaluation of function A relative to particle a (see figure 1). General expressions of kernels are given in [Monaghan (1992)] and [Morris, Fox, and Zhu (1997)]. Different types of kernel interpolation are provided in [Vignjevic, Vuyst, and Gourma (2001)] as well as kernel improvement regarding consistency in [Vignjevic, Reveles, and Campbell (2006)]. In most SPH codes, spline kernels are used and we consider here the fourth order spline kernel, represented on figure 2.

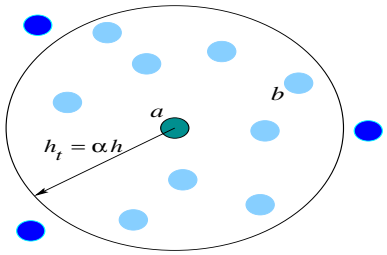

Figure 1: Neighbours of particle a with a compact support kernel.

The interpolant of the function A established according to equation (16) is differentiable provided

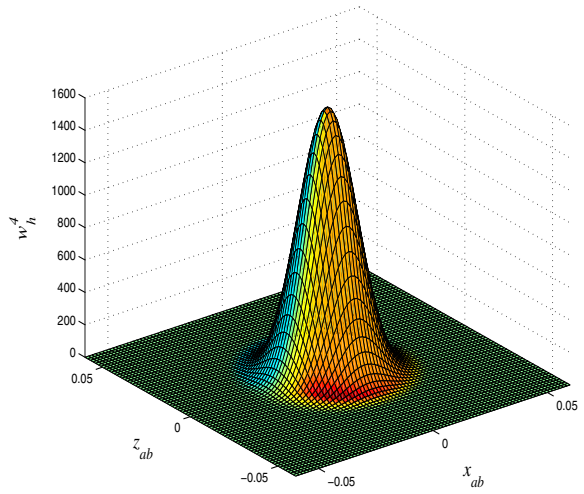

Figure 2: Representation of the fourth order spline kernel with $x_{ab} = x_a - x_b$ and $z_{ab} = z_a - z_b$.

the kernel function is also differentiable. Then, the gradient of a scalar field A relative to particle a can be written

$$(\nabla A)_a = \sum_b \frac{m_b}{\rho_b} A_b \nabla_a w_h(r_{ab}) \tag{17}$$

where $\nabla_a w_h(r_{ab})$ denotes the kernel gradient with respect to a-coordinates. One can notice that there is no need to use a grid to evaluate the gradient of a scalar field since it is a function of the kernel gradient which is analytically known. This SPH feature is essential and very attractive. As in finite-differences methods, the gradient of a scalar field A can be written in several ways in SPH formalism [Monaghan (1992)]. Among others, the following symmetric form

$$(\nabla A)_a = \frac{1}{\rho_a} \sum_b m_b (A_b - A_a) \nabla_a w_h(r_{ab}) \tag{18}$$

or the following assymetric one

$$(\nabla A)_a = \rho_a \sum_b m_b \left(\frac{A_a}{\rho_a^2} + \frac{A_b}{\rho_b^2} \right) \nabla_a w_h(r_{ab}) \tag{19}$$

Derivations of these expressions are provided in [Monaghan (1992)]. In the same way, several forms of the divergence of a vector field could be established [Issa (2004)].

Since we deal here with nearly incompressible (characterised by density fluctuations less than 1 %) turbulent flows, a possible set of weakly compressible Reynolds equations in SPH formalism are herein presented.

3.2 SPH weakly compressible Reynolds equations

Modified equation (1) and equation (5) are used to derive a SPH form of Reynolds equations with the eddy viscosity assumption. From a formalistic point of view, they are identical to the classical SPH Navier-Stokes equations, except that

- pressure and velocities are considered as averaged values
- the kinematic viscosity is increased by the eddy viscosity

Consequently, for particle a, the averaged continuity equation can be written

$$\frac{d\rho_a}{dt} = \sum_b m_b \langle \mathbf{u} \rangle_{ab} \nabla_a w_h(r_{ab}) \tag{20}$$

with $\rho_a \approx \langle \rho \rangle_a$ since nearly incompressible flows are here investigated. $\langle \mathbf{u} \rangle_a$ corresponds to the averaged velocity relative to particle a and $\langle \mathbf{u} \rangle_{ab}$ denotes the quantity $\langle \mathbf{u} \rangle_a - \langle \mathbf{u} \rangle_b$ The r.h.s. of equation (20) is a SPH form of the velocity divergence according to the general methodology presented in section 3.1. An SPH form of the averaged momentum equation (2) is

$$\frac{d\langle \mathbf{u} \rangle_a}{dt} = -\sum_b m_b \left(q_{a,b}^{pres} + q_{a,b}^{visc} \right) \nabla_a w_h(r_{ab}) + \mathbf{F}_a^e \tag{21}$$

with

$$q_{a,b}^{pres} = \frac{\langle p \rangle_a}{\rho_a^2} + \frac{\langle p \rangle_b}{\rho_b^2} \tag{22}$$

corresponding to the pressure gradient term and

$$q_{a,b}^{visc} = -8 \frac{\nu_{T,a} + \nu_{T,b}}{\rho_a + \rho_b} \frac{\langle \mathbf{u} \rangle_{ab} . \mathbf{r}_{ab}}{r_{ab}^2 + \eta^2} \tag{23}$$

corresponding to the viscous term [Monaghan (1992)]. which has here been modelled through

the classical artificial term introduced by Monaghan [Monaghan (1992)] with $\nu_{T,a}$ corresponding to the eddy viscosity attached to particle a (the kinematic viscosity has here been neglected). $\mathbf{r}_{ab}$ denotes the vector $\mathbf{r}_a - \mathbf{r}_b$ while the parameter η (equals to $0.1h$) has been introduced in order to avoid zero denominator. The averaged pressure $\langle p \rangle_a$ is defined by the following filtered state equation

$$\langle p \rangle_a = \frac{\rho_0 c_0^2}{\gamma} \left[\left(\frac{\rho_a}{\rho_0} \right)^{\gamma} - 1 \right] \tag{24}$$

where ρ_0 and c_0 respectively denote the reference density (1000 $kg.m^{-3}$ for water) and a numerical speed of sound. The γ coefficient is equal to 7 for water [Monaghan (1992)], which makes pressure strongly respond to density. Consequently, when particles are getting too close to each other, their pressure will highly increase and will repell these particles from each other through the pressure gradient term. Due to this equation, it comes that pressure automatically goes to zero when density equals the reference density (for instance near a free surface). In order to deal with a nearly incompressible flow (characterised by density fluctuation less than 1 %), the numerical speed of sound should be at least ten times higher than the maximum velocity of the flow [Morris, Fox, and Zhu (1997)].

3.3 SPH eddy viscosity models

In this subsection, turbulent closure models presented in section 2 are applied to SPH. It will be shown that the consitutive equations like (7) remain unchanged while the governing PDE (9) needs to be written in SPH formalism.

3.3.1 An SPH Mixing length model

Considering the mixing length model (7), the eddy viscosity $\nu_{T,a}$ for each fluid particle a is expressed by

$$\nu_{T,a} = L_{m,a}^2 S_a \tag{25}$$

$L_{m,a}$ corresponds to the value of the mixing length at the position occupied by particle a while the velocity gradients required to calculate the rate-of-strain S_a of particle a are estimated through the following symmetric form

$$\left. \frac{\partial \langle u_i \rangle}{\partial x_j} \right|_a = -\frac{1}{\rho_a} \sum_b m_b \langle \underline{u} \rangle_{ab} \otimes \nabla_a w_h(r_{ab}) \tag{26}$$

3.3.2 An SPH k model

With an SPH k model, the eddy viscosity $\nu_{T,a}$ for each fluid particle a is expressed by

$$\nu_{T,a} = C_\mu \frac{k_a^2}{\varepsilon_a} \tag{27}$$

where k_a and ε_a respectively correspond to the turbulent kinetic energy and the dissipation rate for particle a. The following k-transport equation (9) has been written in SPH formalism as

$$\frac{dk_a}{dt} = \underbrace{\sum_b \frac{m_b}{\rho_b} \frac{\nu_{T,a} + \nu_{T,b}}{\sigma_k} \frac{k_{ab} \mathbf{r}_{ab}}{r_{ab}^2 + \eta^2} . \nabla_a w_h(r_{ab})}_{diffusion} + \underbrace{P_a}_{production} - \underbrace{\varepsilon_a}_{dissipation} \tag{28}$$

where $k_{ab} = k_a - k_b$. The diffusion term was written in the same form as the viscous diffusion term developed by Monaghan, as achieved for the temperature conductivity in [Cleary and Monaghan (1999)]. The production term P_a can be modelled according to

$$P_a = C_\mu \frac{k_a^2}{\varepsilon_a} S_a^2 \tag{29}$$

or

$$P_a = min\left(\sqrt{C_\mu}, C_\mu \frac{k_a}{\varepsilon_a} S_a^2 \right) k_a S_a^2 \tag{30}$$

To close the system, the condition (12) for ε_a is used, according to

$$\varepsilon_a = C_\mu^{3/4} \frac{k_a^{3/2}}{L_{m,a}} \tag{31}$$

3.4 Temporal integration

All previous SPH equations are integrated in time with a classical one order Euler scheme according to a time step estimated by

$$\delta t = \min\left(\delta t_{forces}, \delta t_{CFL}, \delta t_{visc}\right) \tag{32}$$

where

$$\delta t_{CFL} = 0.4\frac{h}{c_0} \tag{33}$$

corresponds to a CFL condition which imposes that the time step δt_{CFL} is less or equal to the convection time on the length h relative to the spatial discretisation.

$$\delta t_{forces} = 0.25 \min_a \sqrt{\frac{h}{|\mathbf{f}_a|}} \tag{34}$$

ensures that particles do not get too close to each other during the integration of their movement [Morris, Fox, and Zhu (1997)]. $\underline{f}_a$ denotes the internal and external forces associated to particle a (i.e. the magnitude of the r.h.s. of the momentum equation).

$$\delta t_{visc} = 0.125\frac{h^2}{\nu} \tag{35}$$

This viscous criterion must be taken into account to make the time step inferior to the viscous phenomenon time scale [Morris, Fox, and Zhu (1997)].

3.5 Boundary conditions

3.5.1 Wall modelling

Walls are here modelled with solid particles called edge particles. Moreover, in order to ensure the impermeability of the wall, three layers of dummy particles are added under the wall: the density of edge and dummy particles evolve thanks to the contribution of fluid particles through the averaged continuity equation (20). Indeed, when the fluid particle a is linked to the edge or dummy particle b, the b-contribution to the evolution of a-density is equal to (see equation (20))

$$m_b \langle \mathbf{u} \rangle_{ab} \nabla_a w_h\left(r_{ab}\right) \tag{36}$$

As particle b is also linked to fluid particle a, the contribution of particle a to the evolution of b-density is also given by equation (36), since the continuity equation (20) is symmetric with respect to a and b subscripts. The averaged pressure of edge and dummy particles are then computed with the averaged state equation and these particles are involved in the averaged pressure gradient relative to fluid particles in the momentum equation. These wall conditions also enable a perfect impermeability of the wall in rapid dynamic phenomena such as dam breaking. Contrary to the repulsive forces commonly used in SPH to represent walls [Monaghan (1992)], the present formulation does not introduce any ad hoc coefficient. Moreover, in contrast to traditional mirror particles used in most SPH codes, the method proposed here considers fixed particles and can easily be implemented even for curved walls. It is also practical to model moving wall, as achieved in the following.

3.5.2 Turbulent boundary conditions

For turbulent flows, edge particles represent fluid particles immediately located at the bottom of the turbulent boundary layer. Their gravitational center is hence placed at $z = \delta$, where δ corresponds to a small distance to the wall larger than the viscous sublayer thickness, typically $\delta r/10$ with δr corresponding to the averaged initial particle spacing. In some Eulerian methods using cell vertex discretisation, although the first node is exactly located on the wall, the velocity at that point is non-zero and assumed to correspond to the value at the position δ. This means that the flow domain for a channel of a height H for instance is $[-\delta, H]$ and the computational domain $[0, H]$ (the wall is "pushed back"). The $-\delta$ offset is then negligible [Issa (2004)]. Prescribing turbulent wall boundary conditions with this approach requires wall functions, which give theoretical values of physical quantities in the vicinity of a wall. Although this method can be criticized for adverse pressure driven flows, it was shown to be efficient for simple shear flows in traditional Eulerian codes and was presented and used by the authors [Violeau and Issa (2006)]. The following

wall functions require the estimation of a friction velocity u_{*a} relative to each edge particle a, estimated through the following procedure:

1. For each edge particle a, a fictitious point M located at a distance Δ from a on the normal to the wall (see figure 3) is defined.

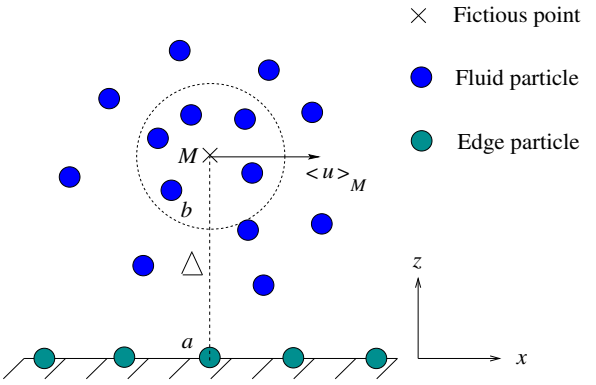

Figure 3: Computation of the friction velocity u_*.

2. The averaged axial velocity at M is computed with the classical following SPH relation

$$\langle u\rangle_M = \sum_b \frac{m_b}{\rho_b}\langle u\rangle_b w_h(r_{Mb}) \tag{37}$$

where r_{Mb} is the distance between fictitious point M and particle b.

3. $\langle u\rangle_M$ should verify the following log-law for a smooth wall

$$\langle u\rangle_M = u_{*a}\left[\frac{1}{\kappa} ln \frac{(\delta+\Delta)\,u_{*a}}{\nu} + B\right] \tag{38}$$

The friction velocity u_{*a} is then obtained by iterating. The constant B is equal to 5.2 $\pm$ 0.74 [Shi, Thomas, and Williams (2000)] and the Von Karman κ equals to 0.41. For a rough wall characterised by a roughness scale ξ, the relation

$$\langle u\rangle_M = u_{*a}\left[\frac{1}{\kappa} ln \frac{(\delta+\Delta)}{\xi} + D\right] \tag{39}$$

directly gives the value of u_{*a} with $D = 8.5$ [Viollet, Chabard, Esposito, and Laurence (1998)].

The edge particle averaged tangential velocity is then computed according to

$$\langle u\rangle_{edge} = u_{*a}\left[\frac{1}{\kappa} ln \frac{\delta u_{*a}}{\nu} + B\right] \tag{40}$$

for a smooth wall and

$$\langle u\rangle_{edge} = u_{*a}\left[\frac{1}{\kappa} ln \frac{\delta}{\xi} + D\right] \tag{41}$$

for a rough wall. It has been shown in [Issa (2004)] that the estimation of u_{*a} is very close to the theoretical value u_* in both cases for a turbulent steady open channel characterised by a constante slope. Near a wall, k-Dirichlet boundary conditions are prescribed according to

$$k_a = \frac{u_{*a}^2}{\sqrt{C_\mu}} \tag{42}$$

4 Plunging breaking solitary wave simulation

Several types of breaking waves are commonly described in the literature - spilling, surging, collapsing, and plunging breaking [Li and Raichlen (2003)]. A photograph of a typical plunging breaking solitary wave is shown on figure 4 just after the plunging jet reaches the free surface. For the slopes, waves and depths considered here, plunging breaking waves are investigated.

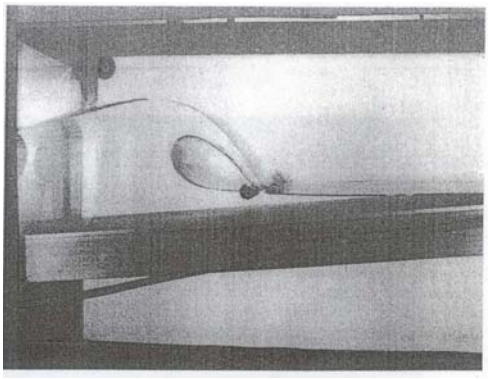

Figure 4: Typical plunging breaking solitary wave showing initiation of slashup [Li and Raichlen (2003)].

4.1 Classical solitary wave generation [Hughes (1993)]

In order to generate the solitary wave represented on figure 5, we consider a piston-type wave board moving on one side of a flume with a flat bottom followed by a gentle slope (see also figure 6). All equations presented in this part are derived from [Hughes (1993)]. The displacement $X_0(t)$ of the wave board has to evolve over the range $-\infty < t < +\infty$ according to:

$$X_0(t) = \frac{H}{Kd} tanh\left[K\left(Ct - X_0\right)\right] \tag{43}$$

where

$$K = \sqrt{\frac{3H}{4d^3}} \tag{44}$$

and

$$C = \sqrt{g\left(d+H\right)} \tag{45}$$

The velocity of the piston is thus evolving according to

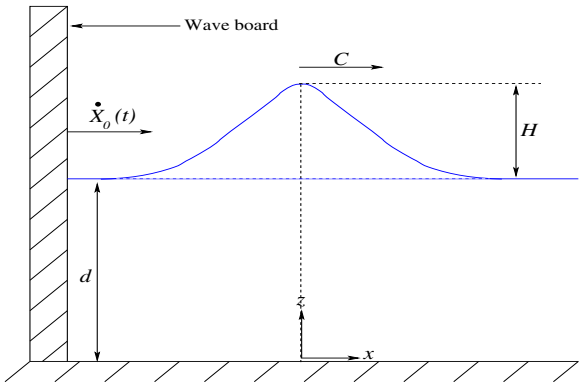

Figure 5: Sketch of the considered solitary wave.

$$\dot{X}_0(t) = \frac{\frac{H}{d} CA}{1 + \frac{H}{d} A} \tag{46}$$

with

$$A = \frac{1}{cosh^2\left[K\left(Ct - X_0\right)\right]} \tag{47}$$

The total stroke S_s, corresponding to the distance between the maximum and minimum displacements of the wave board, is given by

$$S_s = \sqrt{\frac{16Hd}{3}} \tag{48}$$

Goring [Goring (1979)] and Goring and Raichlen [Goring and Raichlen (1980)] compared such laboratory generated solitary waves to the classical wave theories: they reported fairly good agreement over the entire wave form for large waves ($H/d \approx 0.6$) and good agreement for small amplitude solitary wave ($H/d \approx 0.15$).

4.2 Plunging breaking solitary wave experiments [Li and Raichlen (2003)]

By using a simple plane beach, important characteristics of breaking waves can be studied in the laboratory. Indeed, the results for the simple two-dimensional case of a solitary wave propagating in a constant depth and impinging on a plane sloping beach can yield results that are useful for three-dimensional numerical modeling of coastal sites. A schematic of the solitary wave runup experiments achieved in [Li and Raichlen (2003)] is presented on figure 6. Experiments were conducted with this arrangement for a slope of 1:15 and waves were generated using a programmable vertical bulkhead wave generator which moved according to the classical solitary wave theory previously introduced.

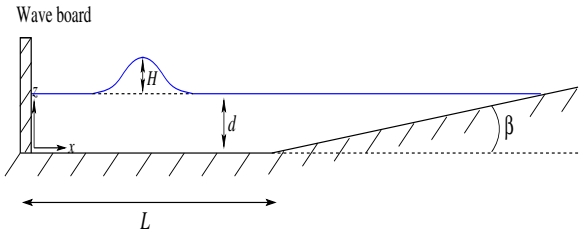

Figure 6: Definition sketch for plunging breaking solitary wave runup [Li and Raichlen (2003)].

4.3 Solitary breaking wave modelling

The system presented on figure 6 is here numerically considered with dhe dimension L, H and

d in meters respectively equal to 5, 0.2 and 0.5. Approximately 350 000 particles initially spaced by $2,5.10^{-3}$ m are considered, as represented on figure 7. In order to generate a plunging breaking solitary wave characterised by $H/d = 0.4$, the velocity of edge and dummy particles defining the wave board evolves according to equation (46) along a distance given by (48). All turbulent boundary conditions relative to edge particles, including velocity, are computed by considering a rough wall characterised by a roughness scale ξ of 0.01 m, according to the method presented in part 3.5.2. Most of scientists consider that waves can be modelled without viscous forces. This is meaningfull in first approximation when considering propagation, which is essentially driven by pressure forces. However, we are now reproducing a breaking wave involving high strains and surface deformation. The above-mentioned turbulence models are then used in order to correctly capture the shape of the free surface and the wave velocity during and after breaking. We will examine the two models presented in section 3.3 (mixing length and k-model) and compare them to a model using a constant (in space and time) eddy viscosity. The value of the latter was estimated from simulations achieved with k-model. For all simulations herein presented, the time step was equal to 3.10^{-5} s and 363 hours were required on a 2.8 GHz Linux PC.

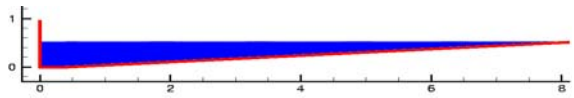

Figure 7: SPH geometry for plunging breaking solitary wave simulations.

4.4 Results

As represented on figure 8, the elevation of the solitary wave generated by SPH is very close to the value of 0.2 m prescribed through the wave board motion. Pictures (a) and (c) of figure 9 represent experimental results presented in [Li and Raichlen (2003)], at two different times corresponding to the formation of the plunging wave.

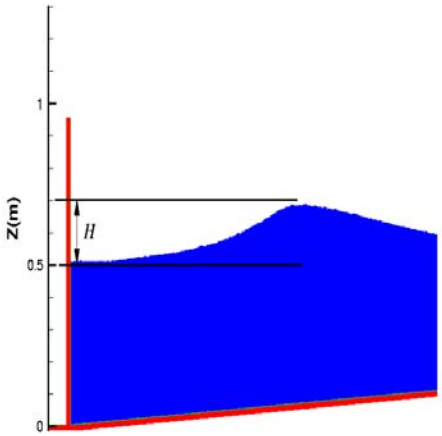

Figure 8: SPH solitary wave generation.

The comparison between experimental and SPH results first reveal that SPH is able to accurately reproduce breaking plunging wave. Moreover, by comparing SPH results obtained with a constant eddy-viscosity, a mixing length model and a k-equation model (bottom pictures of figure 9), one can notice that there is no large discrepancy between the three models. The red solide line depicted on SPH results of figures 9 to 10 corresponds to the experimental free surface shape. For this first step of plunging wave process, it seems as if turbulence modelling is not crucial, the rate of strain being still moderate. Conversely, on experimental pictures of figure 10, the plunging jet impacts the forward face of the wave with a shoreward directed jet generated at the impact point.

This jet impact initiated the splashup/runup process. In this case, the jet is reflected at an angle with the bottom that is greater than the corresponding angle of the incident jet. It is postulated that this splashup is caused by the translation of the impact point of the jet up the slope and its interaction with the front face of the wave [Li and Raichlen (2003)]. SPH simulations of the splashup process initiation (see bottom pictures of figure 10) show that a constant eddy viscosity model does not correctly reproduce this phe-

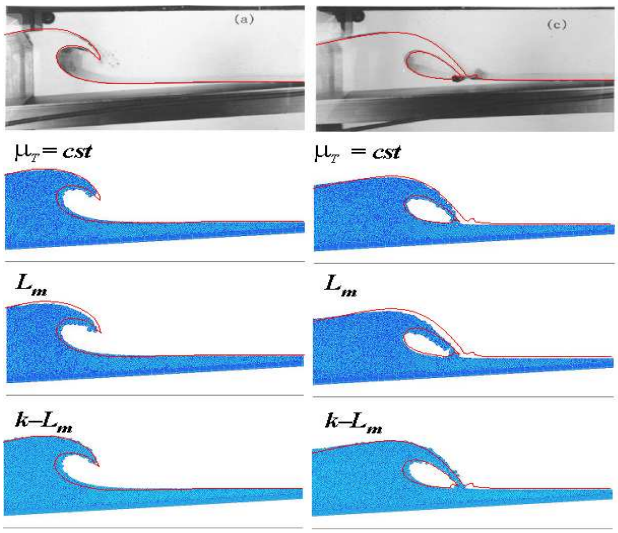

Figure 9: Experimental plunging solitary wave [Li and Raichlen (2003)] (top) and simulated one achieved by SPH with various turbulent closure: constant eddy-viscosity, mixing length and k-model (from top to bottom). The solid lines mimic the experimental free surface.

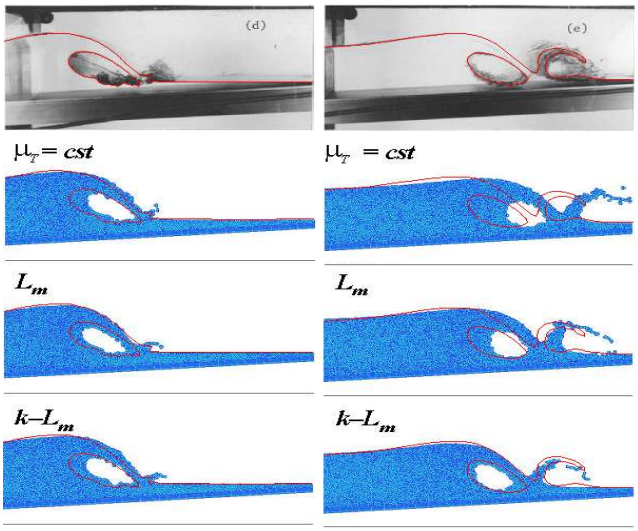

Figure 10: Experimental splashup initiation. Same key as figure 9.

nomenon, while the mixing length model presents slightly better results. In contrast, results obtained with the k-equation model are in good agreement with the experiment. Up to this point, it can be established that turbulence modelling is important to simulate such phenomenon. The reason is that high shear stress generated in the vicinity of the impinging point leads to high turbulent kinetic energy production rate through (29) or (30). Thus, the turbulent kinetic energy - and hence the eddy viscosity - increases a lot and slows down the global motion, which is confirmed by figures 11 and 12 which represents the spatial distribution of k at two different stages (just before and during the splashup process initiation). Splashup development depicted on figure 13 reveals this time that all turbulence models give fairly good results.

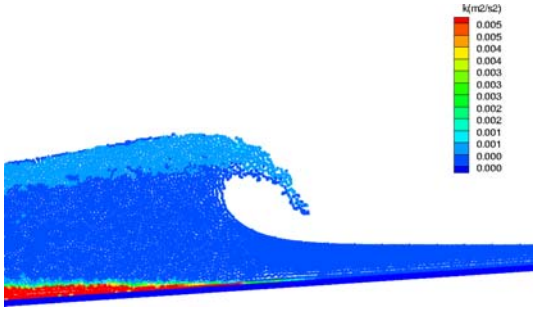

Figure 11: Turbulent kinetic energy distribution before breaking.

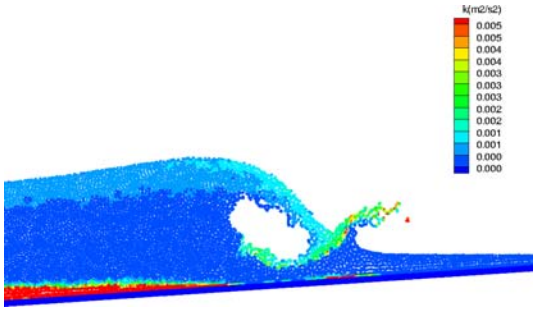

Figure 12: Turbulent kinetic energy distribution after breaking.

As the incident wave moves shoreward, the shape of the splashup (reflected) jet changes and curves

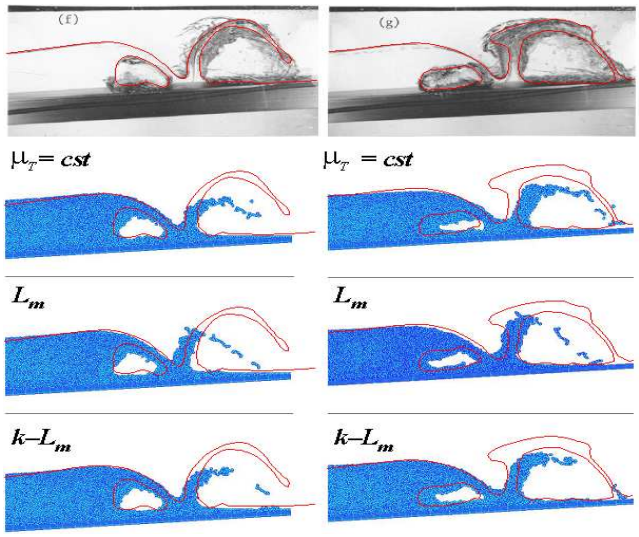

Figure 13: Experimental splashup development. Same key as figure 9.

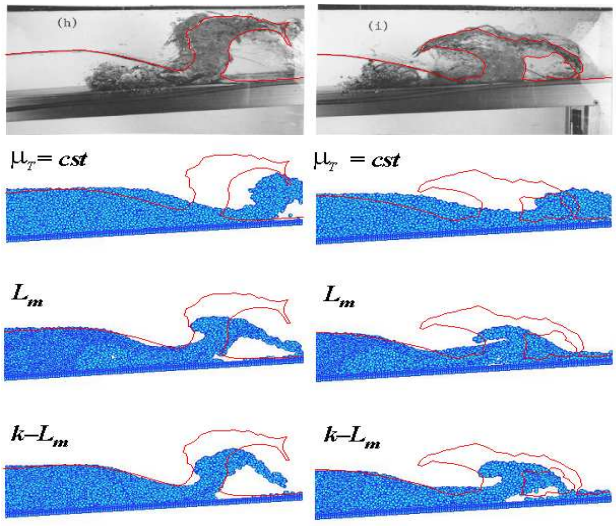

Figure 14: Experimental reflected wave. Same key as figure 9.

back toward the incident wave. Finally, the incident jet disappears and the reflected jet ("counter-breaking") collapses. Once again, comparisons between experimental and numerical results of figure 14 proove that a constant eddy viscosity model is not accurate enough to reproduce the reflected wave. The other models are slightly better but have to be improved, specially regarding wall treatment. The reasons for which even the most sophisticated model presented here fails in predicting the last stages with accuracy may now be evoked. First of all, a two-equation model (*e.g.* the $k-\varepsilon$ model) as presented in [Violeau and Issa (2006)] should be more appropriate to estimate the dissipation rate ε certainly crucial in this flow. Then, one could argue that the Boussinesq's assumption (3) is too poor to capture the complex turbulent stresses involved in the splash-up: high rate of strain and curvature effects would require a non-linear $k-\varepsilon$ model (namely an Explicit Algebraic Reynolds Stress Model) as presented in [Violeau and Issa (2006)]. Finally, one should mention the fact that no free-surface boundary condition regarding the turbulent kinetic energy were prescribed. Recent simulations have shown that imposing a zero-value of k on the free surface slightly improves the prediction of its shape. More generally, interactions between free-surfaces and turbulence (in terms of anisotropy of Reynolds stresses for instance) remain an open field for which theoretical developments should be done in order to apply a method like SPH to very complicated flows.

5 Conclusion

The ability of SPH to accurately reproduce solitary wave with a classical wave board has here been revealed. The surface elevation of the solitary wave is very close to the theoretical value. In the first steps of the process, turbulent effects do not play a prominent part, which justifies the fact that turbulence modelling has been neglected for this step. SPH is also capable of reproducing plunging breaking wave: free surface shape comparisons with experimental results are very satisfactory. Turbulent models remain unuseful until the splash-up generation. Contrary to

this, splashup modelling requires accurate modelling of turbulent effects: it has been shown here that a constant eddy viscosity model gives poor results during splashup initiation while mixing length and k-equation model give much better comparisons. However, the splashup development and the reflected wave which occured at the end of the process are not perfectly represented with SPH, even with turbulent models. The first results introduced through this paper have to be improved, from a numerical and physical point of view: pressure calculation through the classical state equation gives most of the time numerical instabilities, which may be smoothed out by a fully incompressible algorithm [Lo and Shao (2002)]. Moreover, splashup developement and reflected wave may require additional developments based on non-linear $k-\varepsilon$ models accounting for free surface effects. It is also clear that representing this kind of flow with a two-phase simulation involving air, thus allowing to model the influence of air entrainment during the breaking, should increase the quality of the presented results.

References

Cleary, P. W.; Monaghan, J. J. (1999): Conduction modelling using smoothed particle hydrodynamics. *Journal of Computational Physics*, vol. 148.

Dalrymple, R. A.; Rogers, B. D. (2006): Numerical modeling of water waves with the SPH method. *Coastal Engineering*, vol. 53.

Eggels, J. G. M. (1994): *Direct and Large Eddy Simulation of Turbulent Flow in a Cylindrical Pipe Geometry*. TU/Delft, Aero en Hydrodynamica.

Goring, D. G. (1979): Tsunamis-The Propagation of Long Waves Onto a Shelf. Technical report, Laboratory of Hydraulics and Water Resources, 1979.

Goring, D. G.; Raichlen, F. (1980): The Generation of Long Waves in the Laboratory. Technical report, Proceedings of the 17th Coastal Engineering Conference, 1980.

Guimet, V.; Laurence, D. R. (2002): A linearised turbulent production in the $k-\varepsilon$ model for engineering applications. Technical report, Proc. 5th International Symposium on Engineering Turbulence Modelling and Measurements, Mallorca, Spain, 2002.

Hughes, S. A. (1993): *Physical models and laboratory techniques in coastal engineering*. World Scientific.

Issa, R. (2004): *Numerical assessment of the Smoothed Particle Hydrodynamics gridless method for incompressible flows and its extension to turbulent flows*. University of Manchester.

Launder, B. E.; Spalding, D. B. (1972): *Mathematical models of turbulence*. Academic Press, London.

Lesieur, M. (1997): *Turbulence in fluids*. Kluwer.

Li, Y.; Raichlen, F. (2003): Energy balance model for breaking solitary wave runup. *Journal of waterway, port, coastal and ocean engineering*, vol. 47, no. 2, pp. 47–59.

Lo, E. Y. M.; Shao, S. (2002): Simulation of near-shore solitary wave mechanics by an incompressible SPH method. *Applied Ocean Research*, vol. 24.

Métais, O. (2001): Turbulence : modelling and numerical simulation. Technical report, Insitut National Polytechnique de Grenoble, 2001.

Monaghan, J. J. (1992): Smoothed Particle Hydrodynamics. *Annu. Rev. Astron. Astrophy.*, vol. 30.

Morris, J. P.; Fox, P. J.; Zhu, Y. (1997): Modelling low Reynolds Number Incompressible Flows Using SPH. *Journal of Computational Physics*, vol. 136.

Pope, S. B. (2000): *Turbulent flows*. Cambridge University Press.

Shi, J.; Thomas, T. G.; Williams, J. J. R. (2000): Free-Surface Effects in Open Channel

Flow at Moderate Froude and Reynold's Numbers. *Journal of Hydraulic Research*, vol. 38, no. 6, pp. 465–474.

Vignjevic, R.; Reveles, J. R.; Campbell, J. (2006): SPH in a Total Lagrangian Formalism. *CMES: Computer Modeling in Engineering and Sciences*, vol. 14, pp. 181–198.

Vignjevic, R.; Vuyst, T. D.; Gourma, M. (2001): On interpolation in SPH. *CMES: Computer Modeling in Engineering and Sciences*, vol. 2, pp. 319–336.

Violeau, D.; Issa, R. (2006): Numerical modelling of complex turbulent free surface flows with the SPH method: an overview. *International Journal for Numerical Methods in Fluids*, vol. in press.

Violeau, D.; Picon, S.; Chabard, J.-P. (2002): Two Attempts of Turbulence Modelling in Smoothed Particle Hydrodynamics. *Advances in Fluid Modelling and Turbulence Measurements*.

Viollet, P. L.; Chabard, J. P.; Esposito, P.; Laurence, D. (1998): *Mécanique des fluides appliquée. Ecoulements incompressibles dans les circuits, canaux, rivières, autour de structures et dans l'environnement*. Presses de l'Ecole Nationale des Ponts et Chaussées.

Welton, W. C. (1998): Two-dimensional PDF/SPH Simulations of Compressible turbulent flows. *Journal of Computational Physics*, vol. 139.